INTERNATIONAL JOURNAL FOR NUMERICAL METHODS IN FLUIDS, VOL. 9, 275–287 (1989)

A FINITE ELEMENT ANALYSIS OF THE STEADY LAMINAR ENTRANCE FLOW IN A 90° CURVED TUBE

F. N. VAN DE VOSSE, A. A. VAN STEENHOVEN, A. SEGAL* AND J. D. JANSSEN

Department of Mechanical Engineering, Eindhoven University of Technology, Den Dolech 2, Postbus 513, The Netherlands,
*Department of Mathematics and Informatics, *Delft University of Technology, The Netherlands*

SUMMARY

A standard Galerkin finite element penalty function method is used to approximate the solution of the three-dimensional Navier–Stokes equations for steady incompressible Newtonian entrance flow in a 90° curved tube (curvature ratio $\delta = 1/6$) for a triple of Dean numbers ($\kappa = 41$, 122 and 204). The computational results for the intermediate Dean number ($\kappa = 122$) are compared with the results of laser–Doppler velocity measurements in an equivalent experimental model. For both the axial and secondary velocity components, fair agreement between the computational and experimental results is found.

KEY WORDS Curved pipe flow Entrance flow Finite element method Penalty function method Experimental validation

1. INTRODUCTION

The steady entrance flow in a curved tube has been analysed as a first step towards fully three-dimensional analyses of the flow in arterial bifurcation models. The curved tube geometry has been choosen for two main reasons. First, the flow in bifurcations shows properties resembling the entrance flow in a curved tube.[1–3] Secondly, the computations of the flow in a curved tube form a non-trivial way to evaluate the numerical method for three-dimensional flow including non-negligible secondary flow components.

If the Navier–Stokes equations are rewritten in an orthogonal curvilinear toroidal co-ordinate system (see Figure 1), two important dimensionless parameters are found:[4] the curvature ratio

$$\delta = a/R \tag{1}$$

and the Dean number

$$\kappa = Re\sqrt{\delta}, \tag{2}$$

with a the radius of the tube, R the curvature radius and Re the Reynolds number based on the diameter of the tube and the mean axial velocity; $Re = WD/\nu$, with W the mean axial velocity and ν the kinematic viscosity. The Dean number can be interpreted as the ratio of the square root of the product of the convective inertial forces and centrifugal forces to the viscous forces, i.e.

$$\kappa = \frac{\sqrt{[\frac{1}{2}(W^2/2a)(W^2/R)]}}{\nu W/4a^2}. \tag{3}$$

In this study a curvature ratio $\delta = 1/6$ has been chosen corresponding to the geometry of the

0271–2091/89/030275–13$06.50

Received 5 November 1987
Revised 9 May 1988

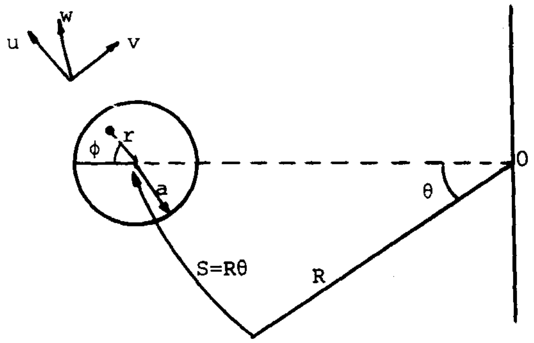

Figure 1. Toroidal co-ordinate system (r, ϕ, θ)

human carotid artery bifurcation.[5] With Reynolds numbers in the physiological range $100 < Re < 800$, this leads to Dean numbers in the range $40 < \kappa < 330$.

Experimental analyses in the ranges of δ and κ considered, using a uniform inlet flow profile, were made by Olson,[1] Agrawal *et al.*,[6] Choi *et al.*[7] and Olson and Snyder.[8,9] In the case of a uniform inlet flow, immediately downstream of the entry in the bend a secondary flow is set up, which is dominated by the build-up of an axial boundary layer. Further downstream, two helical vortices develop as a result of the interaction between convective, centrifugal and viscous forces. Considering laminar flow, a fully developed parabolic velocity profile is a more convenient inlet flow for several reasons. In contrast with a uniform inlet flow, fully developed inlet flow can be achieved more easily in an experimental set-up and is well defined. The importance of a well defined inlet flow is underlined by the observations made by Olson and Snyder,[9] who found a far-downstream influence of the inlet condition. Furthermore, a fully developed inlet flow is more convenient for numerical analyses, since leading edge singularities are avoided. As far as is known, the development from a parabolic entry velocity profile has only been reported by Olson,[1] who presented the development of the axial velocity profiles in the plane of symmetry of the bend ($1/16 < \delta < 1/4{\cdot}66$ and $45 < \kappa < 756$), by Bovendeerd *et al.*,[10] who presented both axial and secondary velocity distributions at several cross-sections ($\delta = 1/6$ and $\kappa = 286$), and finally by Smith,[11] who derived an analytical approximation of the problem. Other numerical flow investigations have been carried out only for uniform inlet flows.[12-16] They used finite difference or analytical approximations, transforming the problem into toroidal co-ordinates. In this study a Cartesian co-ordinate system is used in order to incorporate straight inflow and outflow tubes in the numerical model and to enable a generalization of the method for other 3D geometries.

A finite element formulation of the Navier–Stokes equations (see e.g. Cuvelier *et al.*[17]) is used and applied to the entrance flow in a curved tube developing from a parabolic entry velocity profile. To validate the numerical method, for one value of the Reynolds number ($Re = 300$) the computational results are compared with the results of laser–Doppler measurements. First, the finite element method used will be dealt with. Then, the results of the calculations will be presented and compared with the results attained from experiments. Only a global description will be given of the experimental method, for which the reader is referred to Bovendeerd *et al.*[10] Finally, the results will be discussed and some concluding remarks will be made.

2. NUMERICAL METHOD

Governing equations

The Navier–Stokes equations for steady incompressible flow are given by the momentum equations together with the continuity equation. For a bounded domain $\Omega \in R^3$ with boundary Γ they read

$$\rho(\mathbf{u}\cdot\nabla)\mathbf{u}=\rho\mathbf{f}+\nabla\cdot\boldsymbol{\sigma}, \qquad \nabla\cdot\mathbf{u}=0. \tag{4}$$

Here ρ denotes the density, $\mathbf{u}$ the velocity, $\boldsymbol{\sigma}$ the Cauchy stress tensor and $\mathbf{f}$ the body force. For Newtonian fluids the Cauchy stress tensor can be written as

$$\boldsymbol{\sigma}=-p\mathbf{I}+2\eta\nabla_s\mathbf{u}, \tag{5}$$

with p the pressure, $\mathbf{I}$ the unity tensor, η the dynamic viscosity and $\nabla_s\mathbf{u}$ the rate of strain tensor defined as the symmetrical part of $\nabla\mathbf{u}$.

The following boundary conditions are considered:

$$\begin{aligned}
&\mathbf{u}=\mathbf{g} \quad \text{at } \Gamma_1 \quad (\mathbf{g}\neq\mathbf{0}\text{:inflow condition, } \mathbf{g}=\mathbf{0}\text{:no-slip condition}),\\
&(\boldsymbol{\sigma}\cdot\mathbf{n})=\mathbf{0} \quad \text{at } \Gamma_2 \quad (\text{stress-free outflow condition}),\\
&\left.\begin{array}{ll}(\boldsymbol{\sigma}\cdot\mathbf{n})\cdot\mathbf{t}_1 & =0\\ (\boldsymbol{\sigma}\cdot\mathbf{n})\cdot\mathbf{t}_2 & =0\\ (\mathbf{u}\cdot\mathbf{n}) & =0\end{array}\right\} \quad \text{at } \Gamma_3 \quad (\text{symmetry condition}),
\end{aligned} \tag{6}$$

with $\Gamma_1\cup\Gamma_2\cup\Gamma_3=\Gamma$, $\Gamma_i\subset\Gamma_{j\neq i}=\varnothing$ $(i=1, 2, 3)$, $\mathbf{n}$ the outer normal on Γ and $\mathbf{t}_j$ $(j=1, 2)$ the orthonormal tangential vectors on Γ.

Variational formulation

With the aid of the Hilbert space $L^2(\Omega)=\{v\,|\int_\Omega v^2\,\mathrm{d}\Omega<\infty\}$ and the first-order Sobolev space $H^1(\Omega)=\{v\,|\,v\in L^2(\Omega),\ \partial v/\partial x_i\in L^2(\Omega),\ i=1, 2, 3\}$ the following spaces are introduced:

$$\begin{aligned}
&\mathbf{V}=\{\mathbf{v}\,|\,v_i\in H^1(\Omega),\ \mathbf{v}|_{\Gamma_1}=\mathbf{0},\ (\mathbf{v}\cdot\mathbf{n})|_{\Gamma_3}=0,\ i=1,2,3\},\\
&Q=\{q\,|\,q\in L^2(\Omega)\}.
\end{aligned} \tag{7}$$

For $\mathbf{u}\in\mathbf{H}^1_g(\Omega)$ $(\mathbf{H}^1_g(\Omega)=\{\mathbf{v}\,|\,v_i\in H^1(\Omega),\ \mathbf{v}|_{\Gamma_1}=\mathbf{g},\ \mathbf{v}\cdot\mathbf{n}|_{\Gamma_3}=0\})$ and $p\in L^2(\Omega)$ and for a given $\mathbf{f}\in L^2(\Omega)$, an equivalent variational formulation of equations (4) can be derived as: Find a pair $(\mathbf{u}, p)\in\mathbf{H}^1_g(\Omega)\times L^2(\Omega)$ such that

$$\begin{aligned}
&\int_\Omega[\rho(\mathbf{u}\cdot\nabla)\mathbf{u}]\cdot\mathbf{v}\,\mathrm{d}\Omega=\int_\Omega\rho\mathbf{f}\cdot\mathbf{v}\,\mathrm{d}\Omega+\int_\Omega(\nabla\cdot\boldsymbol{\sigma})\cdot\mathbf{v}\,\mathrm{d}\Omega \quad \forall\mathbf{v}\in\mathbf{V},\\
&\int_\Omega(\nabla\cdot\mathbf{u})q\,\mathrm{d}\Omega=0 \qquad \forall q\in Q.
\end{aligned} \tag{8}$$

Applying Green's formula and substituting equation (5) and boundary conditions (6) yields the weak form: find a pair $(\mathbf{u}, p)\in\mathbf{H}^1_g(\Omega)\times L^2(\Omega)$ such that

$$\begin{aligned}
&\int_\Omega 2\eta(\nabla_s\mathbf{u}\cdot\nabla)\cdot\mathbf{v}\,\mathrm{d}\Omega+\int_\Omega[\rho(\mathbf{u}\cdot\nabla)\mathbf{u}]\cdot\mathbf{v}\,\mathrm{d}\Omega-\int_\Omega p(\mathbf{I}\cdot\nabla)\cdot\mathbf{v}\,\mathrm{d}\Omega=\int_\Omega\rho\mathbf{f}\cdot\mathbf{v}\,\mathrm{d}\Omega \quad \forall\mathbf{v}\in\mathbf{V},\\
&\int_\Omega(\nabla\cdot\mathbf{u})q\,\mathrm{d}\Omega=0 \qquad \forall q\in Q
\end{aligned} \tag{9}$$

Galerkin finite element approximation

In order to discretize the variational problem (9), two finite-dimensional spaces $\mathbf{v}^h \subset \mathbf{V}$ and $Q^h \subset Q$ and two finite-dimensional spaces $\tilde{\mathbf{V}}^h \subset \mathbf{H}_g^1(\Omega)$ and $\tilde{Q}^h \subset L^2(\Omega)$ are defined such that

$$\lim_{h\to 0} \|\mathbf{u}-\mathbf{v}^h\|_{H^1(\Omega)}=0, \qquad \lim_{h\to 0} \|p-q^h\|_{L^2(\Omega)}=0, \tag{10}$$

with

$$\|v\|_{H^1(\Omega)}=\left\{\int_\Omega \left[v^2+\sum_{i=1}^{3}\left(\frac{\partial v}{\partial x_i}\right)^2\right]\mathrm{d}\Omega\right\}^{1/2}, \qquad \|q\|_{L^2(\Omega)}=\left(\int_\Omega q^2\,\mathrm{d}\Omega\right)^{1/2}. \tag{11}$$

The variational problem (9) can then be approximated by: find $\mathbf{u}^h \in \tilde{\mathbf{V}}^h$ and $p^h \in \tilde{Q}^h$ such that

$$\begin{aligned}\int_\Omega 2\eta(\nabla_s\mathbf{u}^h\cdot\nabla)\cdot\mathbf{v}^h\,\mathrm{d}\Omega+\int_\Omega[\rho(\mathbf{u}^h\cdot\nabla)\mathbf{u}^h]\cdot\mathbf{v}^h\,\mathrm{d}\Omega-\int_\Omega p^h(\mathbf{I}\cdot\nabla)\cdot\mathbf{v}^h\,\mathrm{d}\Omega=\int_\Omega \rho\mathbf{f}\cdot\mathbf{v}^h\,\mathrm{d}\Omega \quad & \forall\mathbf{v}^h\in\mathbf{V}^h,\\ \int_\Omega(\nabla\cdot\mathbf{u}^h)q^h\,\mathrm{d}\Omega=0 \quad & \forall q^h\in Q^h.\end{aligned} \tag{12}$$

The existence and uniqueness of a solution of (12) can only be proved for spaces $\mathbf{V}^h$ and Q^h satisfying the so-called Brezzi–Babuska condition,[18, 19] which states that one cannot mix arbitrary spaces for the velocity and pressure approximation.[20, 21] Moreover, the uniqueness of a solution of the Navier–Stokes equations can only be proved for viscosities which are 'sufficiently' large and body forces which are 'sufficiently' small.[22]

Let ϕ_{in} be a basis of space $\tilde{\mathbf{V}}^h$ and ψ_m be a basis of space $\tilde{Q}^h$ ($i=1, 2, 3$, $n=1, \ldots, N$ and $m=1, \ldots, M$), then $\mathbf{u}^h$ and p^h are defined by

$$u_i^h=\sum_{n=1}^{N} u_{in}\phi_{in}, \quad i=1, 2, 3, \qquad p^h=\sum_{m=1}^{M} p_m\psi_m. \tag{13}$$

Substitution of (13) into the variational problem (12) yields the following system of non-linear equations:

$$\mathbf{Su}+\mathbf{N(u)u}+\mathbf{L}^{\mathrm{T}}\mathbf{p}=\mathbf{f}, \qquad \mathbf{Lu}=\mathbf{Q}, \tag{14}$$

with

$$\mathbf{S}=\begin{bmatrix} S^{11} & S^{12} & S^{13}\\ S^{21} & S^{22} & S^{23}\\ S^{31} & S^{32} & S^{33}\end{bmatrix},$$

$$\begin{aligned} S^{ij}(k,l)&=\int_\Omega \eta\left[\sum_{\alpha=1}^{3}\left(\frac{\partial\phi_{ik}}{\partial x_\alpha}\frac{\partial\phi_{jl}}{\partial x_\alpha}\right)\delta_{ij}+\frac{\partial\phi_{ik}}{\partial x_j}\frac{\partial\phi_{jl}}{\partial x_i}\right]\mathrm{d}\Omega,\\ [\mathbf{N(u)u}]_{ik}&=\sum_{j=1}^{3}\int_\Omega \rho\left(\sum_{n=1}^{N} u_{jn}\phi_{jn}\sum_{l=1}^{N} u_{il}\frac{\partial\phi_{il}}{\partial x_j}\right)\phi_{ik}\,\mathrm{d}\Omega,\\ \mathbf{L}&=[L^1 \;\; L^2 \;\; L^3], \qquad L^i(m,l)=-\int_\Omega \psi_m\frac{\partial\phi_{il}}{\partial x_i}\mathrm{d}\Omega,\\ \mathbf{f}&=[\mathbf{f}^1 \;\; \mathbf{f}^2 \;\; \mathbf{f}^3]^{\mathrm{T}}, \mathbf{f}^i(k)=\int_\Omega \rho f_i\phi_{ik}\,\mathrm{d}\Omega,\\ \mathbf{u}&=[\mathbf{u}^1 \;\; \mathbf{u}^2 \;\; \mathbf{u}^3]^{\mathrm{T}}, \qquad \mathbf{u}^i(k)=u_{ik}, \qquad \mathbf{p}(m)=p_m.\end{aligned} \tag{15}$$

Penalty function approach

Direct solution of the set of equations (14) is time- and memory-consuming owing to the fact that zero components appear on the principal diagonal of the coefficient matrix. These zero coefficients are due to the absence of the pressure in the continuity equation and in general require a partial pivoting procedure which disturbs the band structure of the matrix. To overcome this difficulty, the penalty function method is applied by solving, instead of (14),

$$[\mathbf{S}+\mathbf{N}(\mathbf{u}_\varepsilon)+(1/\varepsilon)\,\mathbf{L}^{\mathrm{T}}\mathbf{M}_{\mathrm{p}}^{-1}\mathbf{L}]\mathbf{u}_\varepsilon=\mathbf{f}, \qquad \mathbf{p}_\varepsilon=(1/\varepsilon)\mathbf{M}_{\mathrm{p}}^{-1}\mathbf{L}\mathbf{u}_\varepsilon, \tag{16}$$

with

$$\mathbf{M}_{\mathrm{p}}(k,l)=\int_\Omega \psi_k\psi_l\,\mathrm{d}\Omega, \quad k=1,\ldots,M;\ l=1,\ldots,M. \tag{17}$$

Since the penalty formulation as stated here is obtained from the discrete set of equations (14), the orthogonal projection matrix $\mathbf{M}_{\mathrm{p}}$ ensures that the space Q^h is a proper subspace of Q, and no reduced integration rules are needed to obtain a unique solution of the pressure[5].

Caray and Krishnan[23] showed that for the steady Navier–Stokes equations the solution of (16) converges to the solution of (14) with the following error bound:

$$\|\mathbf{u}_\varepsilon^h-\mathbf{u}^h\|_{H^1(\Omega)}+\|p_\varepsilon^h-p^h\|_{L^2(\Omega)}<C\varepsilon, \tag{18}$$

with C independent of ε. These results are confirmed by the numerical experiments of Reddy.[24] The main advantage of the penalty function method over the direct solution of equations (14) is that the pressure is eliminated from the momentum equations, resulting in a smaller set of equations which can be solved without the demand of pivoting procedures.

The 27-noded hexahedral $(\mathrm{Q}_2-\mathrm{P}_1)$ *element*

A survey of finite elements for the three-dimensional Navier–Stokes equations is given by Fortin[21] and Fortin and Fortin.[25,26] The Brezzi–Babuska condition and the applicability of a penalization formulation (i.e. a discontinuous pressure approximation) are of importance for the choice of an element. The simplest element, which is at least second-order accurate and which satisfies the above mentioned conditions, is the full quadratic velocity–linear pressure $(\mathrm{Q}_2^{(27)}-\mathrm{P}_1)$ element (see Figure 2). Similar to the $(\mathrm{P}_2^+-\mathrm{P}_1)$ element,[27] which has been proved to be successful for the two-dimensional Navier–Stokes equations,[28] the pressure is approximated by its value and its derivatives in the centroid of the element and thereby is discontinuous over the element boundary. The number of unknowns per element is 81 for the velocity and four for the pressure. In the literature only limited experience with three-dimensional elements is reported. With respect to the $(\mathrm{Q}_2-\mathrm{P}_1)$ element the following note can be made:[25,26] since the pressure imposes only four constraints on the 81 degrees of freedom in velocity, the divergence-free condition can perhaps not be applied strongly enough and may lead to too compressible an element. Nevertheless, an $O(h^3)$ accuracy in the velocity approximation was found for a simple test example.[29] In the next section the $(\mathrm{Q}_2-\mathrm{P}_1)$ element will be applied to the flow in a 90° curved tube and the results will be compared with data obtained from laser–Doppler experiments.

3. RESULTS

The entrance flow in a curved tube with curvature ratio $\delta=1/6$ was calculated for $Re=100$, 300 and 500 ($\kappa\approx41$, 122 and 204). To this end, a finite element mesh was generated as depicted in

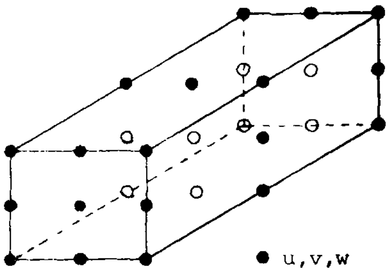

Figure 2. The 27-noded hexahedral (Q_2-P_1) element

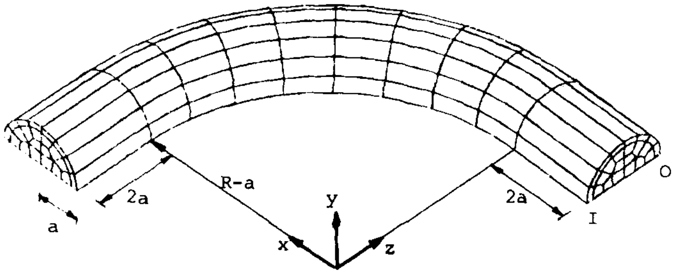

Figure 3. Geometry and finite element mesh as used in the calculations (220 elements, 2205 nodes)

Figure 3. Upstream of the entrance ($\theta=0$) and downstream of the exit ($\theta=\pi/2$) of the 90° bend, an inlet and an outlet section with a length of twice the tube diameter were used. A parabolic axial velocity distribution and zero secondary velocities were imposed as inflow condition, whereas natural (zero normal traction and zero normal strain) outflow conditions were used.

Experiments were performed in a Perspex model with an internal radius of 4 mm and a curvature radius of 24 mm ($\delta=1/6$). The outer surfaces of the model were chosen in such a way that the three velocity components were measured with the optical axis of the laser–Doppler anemometer employed perpendicular to the outer surface.[10] A long inlet section of 0·4 m ensured a fully developed parabolic flow at the entrance of the bend. Also, downstream of the bend a long straight glass pipe was present. The Reynolds number of the flow was kept at $Re=300$ ($\kappa=122$). The velocity components were measured at five cross-sections in the bend ($\theta=0$ ($\pi/8$) $\pi/2$) corresponding with the element boundaries in the finite element mesh (see Figure 3).

Axial velocities

In Figure 4 the development of the axial velocity in the plane of symmetry is given for $Re=100$, 300 and 500. In addition, the measured values of the axial velocity at $Re=300$ are given and indicated by circles. At the first two velocity profiles ($\theta=0$ and $\theta=\pi/16$) hardly any influence of the curvature is visible, although a slight shift towards the inner bend is observable at $\theta=0$. Further downstream, the maximum of the axial velocity profile is shifted towards the outer bend. At higher Reynolds numbers this shift is more pronounced and a plateau in the profiles develops near the inner bend. Only at $Re=100$ does the flow seem to be fully developed at $\theta=\pi/2$. Despite an overall overestimation of the axial velocity (probably due to a measurement inaccuracy of the imposed flow value), the calculations agree well with the experiments at all cross-sections.

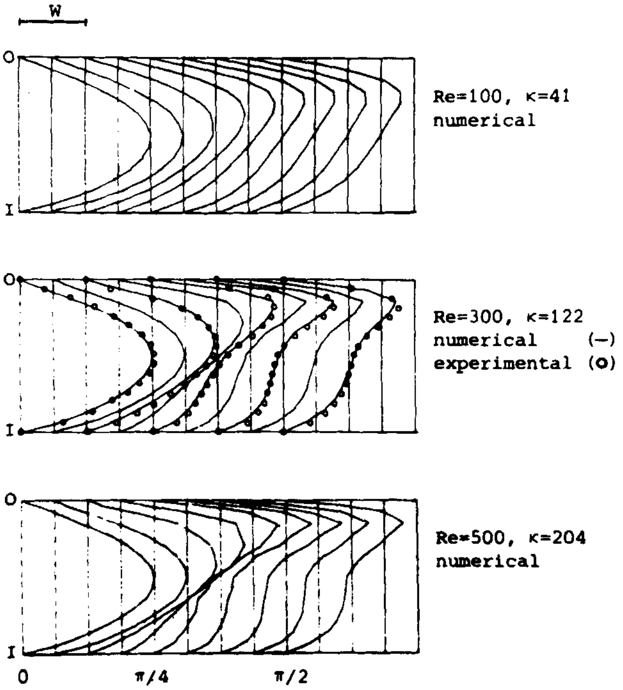

Figure 4. Axial velocity in the plane of symmetry of the curved tube ($\delta = 1/6$) as calculated for $Re = 100, 300$ and 500 ($\kappa = 41$, 122 and 204) and measured (○) for $Re = 300$ ($\kappa = 122$). O, I denote outer and inner bend respectively

In Figure 5 a more complete picture of the axial flow development is given. Here the axial velocity distribution is given by isovelocity contours at several cross-sections in the tube. An almost parabolic axial velocity distribution is observed at $\theta = 0$. This paraboloid, however, is shifted slightly towards the inner bend. The experimental isovelocity contours of the axial velocity component at this axial position show a shift from the 'upper' wall, probably due to the inaccuracy in the determination of the wall position. At $\theta = \pi/8$ the isovelocity contours shift towards the outer bend of the tube and no significant deviation is found for the various Reynolds numbers. Halfway round the bend ($\theta = \pi/4$) the shift towards the outer bend has continued and large wall shear rates occur at the outer bend of the tube. At higher-Reynolds-number flow a 'C-shaped' isovelocity contour is found for the high-velocity region. At the cross-sections $\theta = 3\pi/8$ and $\theta = \pi/2$ the 'C-shaped' contours further develop and for $Re = 100$, at first sight, an almost fully developed axial velocity distribution is found. The agreement between the experiments and the calculations at $Re = 300$ is fair.

Secondary velocities

In Figure 6 the development of the secondary velocity field is given for $Re = 100$, 300 and 500. These velocities are normalized with respect to the mean axial velocity W. At the entrance ($\theta = 0$) the upstream influence of the bend is visible in a unidirectional secondary flow from the outer bend towards the inner bend, which amounts to be about 5% of the mean axial flow. The same upstream influence of the bend was found in the experiments. At $\theta = \pi/8$ a vortex has developed which near the plane of symmetry is directed from the inner bend towards the outer bend, and at the upper wall from the outer bend back to the inner bend. The centre of this vortex is

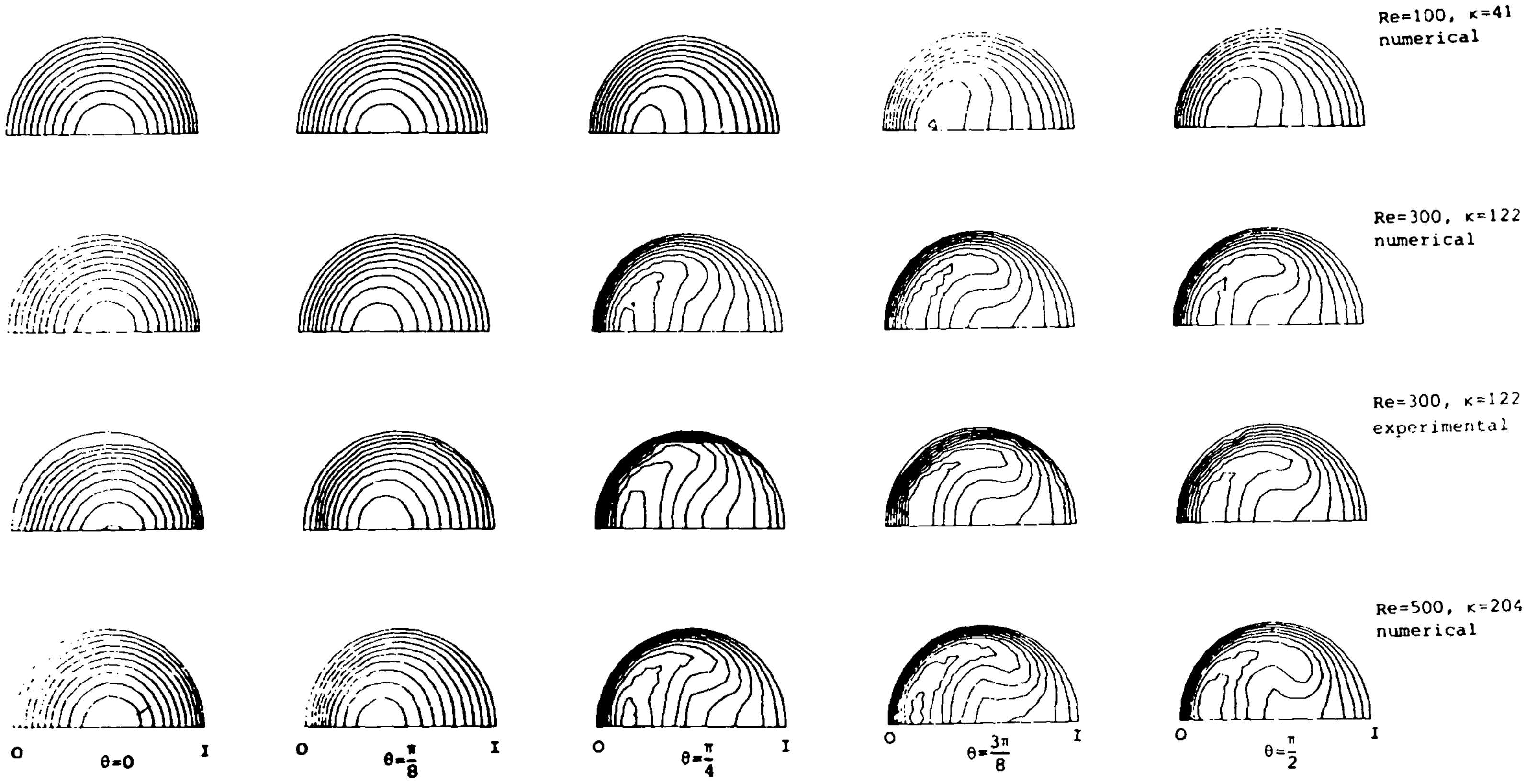

Figure 5. Isovelocity contours (level difference $\Delta w/W = 0{\cdot}2$) of the axial velocity in the curved tube ($\delta = 1/6$) as calculated for $Re = 100$, 300 and 500 ($\kappa = 41$, 122 and 204) and measured for $Re = 300$ ($\kappa = 122$). O, I denote outer and inner bend respectively

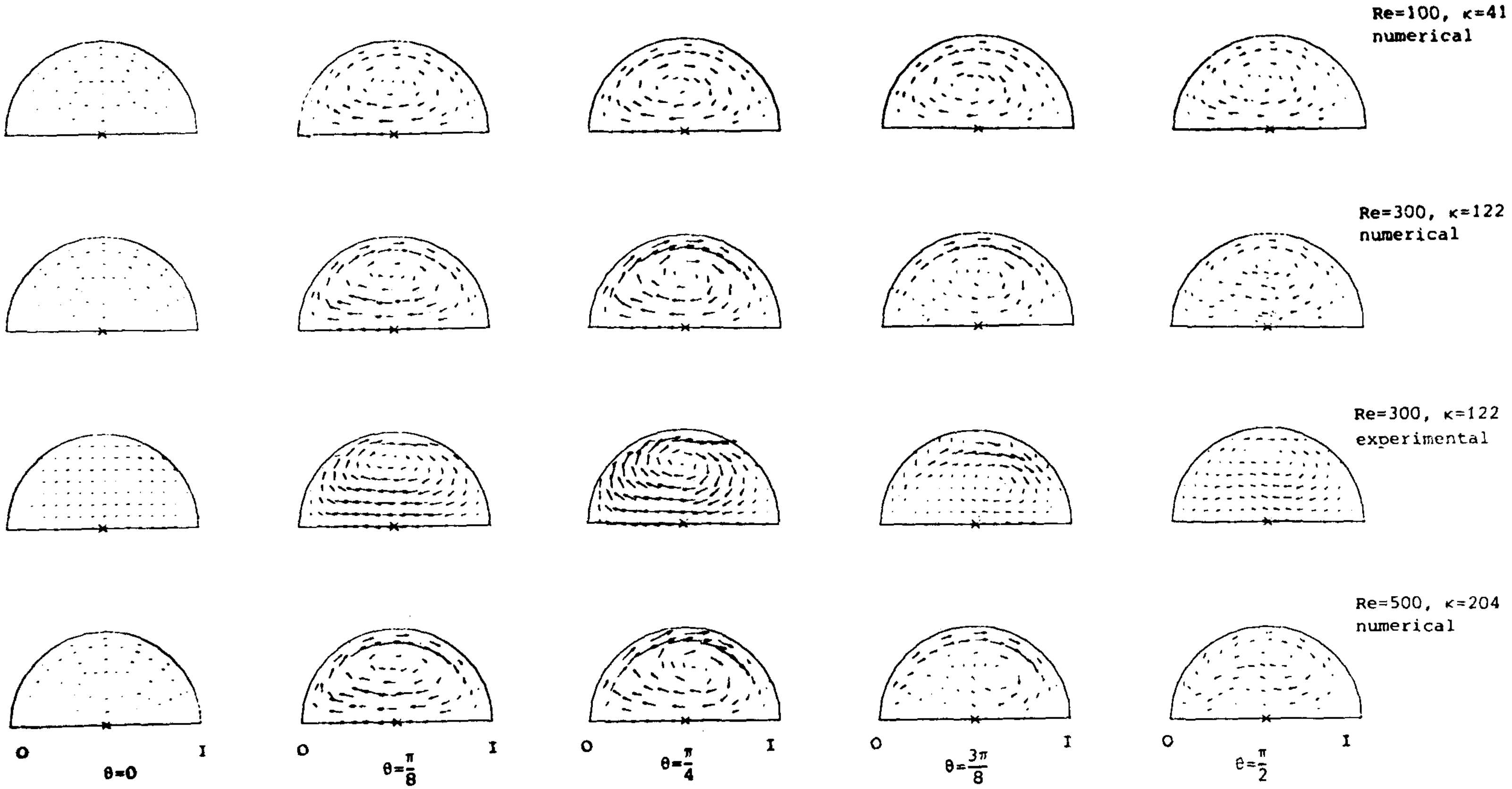

Figure 6. Normalized secondary velocity vectors in the curved tube ($\delta = 1/6$) as calculated for $Re = 100$, 300 and 500 ($\kappa = 41$, 122 and 204) and measured for $Re = 300$ ($\kappa = 122$). O, I denote outer and inner bend respectively

approximately located at ($x/a=0$, $y/a=0{\cdot}65$). Hardly any influence of the Reynolds number on the shape of the vortex is observable at this axial location. However, the normalized secondary velocity components are larger at the higher Reynolds numbers. Although direct comparison with the experiments is difficult because of the different locations at which the velocities are determined, good agreement is found at this axial station. At $\theta=\pi/4$ the layer with circumferential flow along the upper wall has intensified, especially at the higher-Reynolds-number flows. Near the plane of symmetry the secondary velocities are found to be slightly lower than at $\theta=\pi/8$. For $Re=500$ a shift of the vortex centre towards the inner bend is found. Also at this axial station the experiments agree well with the calculations, although in the experimental case the centre of the vortex is observed to be located somewhat closer to the upper wall. Next, at $\theta=3\pi/8$ the influence of the Reynolds number on the secondary flow field is clearly visible. For the low-Reynolds-number case ($Re=100$) the vortex found has approximately the same shape and strength as those found at the two axial locations upstream. For $Re=300$ and $Re=500$, however, the secondary velocities are significantly lower, especially near the plane of symmetry. The centre of the vortex has moved further in the inner bend direction while, in addition, a deformation of the shape of the vortex has taken place. A similar behaviour is found in the experiments. At $\theta=\pi/2$ the same characteristics are found but also an extra outer-bend-directed fluid motion is observed, superimposed on the vortex flow. The same phenomenon is found experimentally.

More quantitative but less detailed information on the secondary flow field can be obtained from the circulation Γ or the mean axial vorticity ξ_c

$$\xi_c=\Gamma/A=\oint_S \mathbf{u}\cdot d\mathbf{s}/A, \tag{19}$$

with S a path along the plane of symmetry and the upper tube wall, surrounding a surface A ($=\pi a^2/2$). Following Olson and Snyder's procedure,[9] this quantity is best used in the dimensionless form

$$\xi_c'=\frac{\xi_c a}{W}\delta^{3/2}. \tag{20}$$

In Figure 7 this dimensionless mean axial vorticity ξ_c' is plotted as a function of θ/δ. Owing to the overall flow to the inner bend at $\theta=0$, the curves start at negative values. Then a large increase is found, coinciding with the development of the secondary vortex. For the higher Reynolds numbers this increase is larger but also reaches its maximum at smaller angles θ. Thereafter, the circulation decreases again to a value which is smaller for larger Reynolds numbers. The upstream effect of the straight outflow tube is expressed as a sudden increase of the circulation. Although the axial and secondary velocity distributions suggest that the flow at $Re=100$ seems to be fully developed at $\theta=\pi/4$, the mean axial vorticity curve in Figure 7 does not reach an asymptotic value. The mean axial vorticity at $Re=300$ as calculated from the experimental data agrees fairly well with the numerically obtained one.

4. DISCUSSION

In the preceding section the results of calculations of the entrance flow in a curved tube have been presented by means of the axial and secondary velocity distributions. The results of the calculations for $Re=300$ agree well with the experimental results. Combining the information described separately in the preceding section, the following remarks are made. At $\theta=0$ the secondary flow is directed towards the inner bend and also the maximum of the axial velocity is

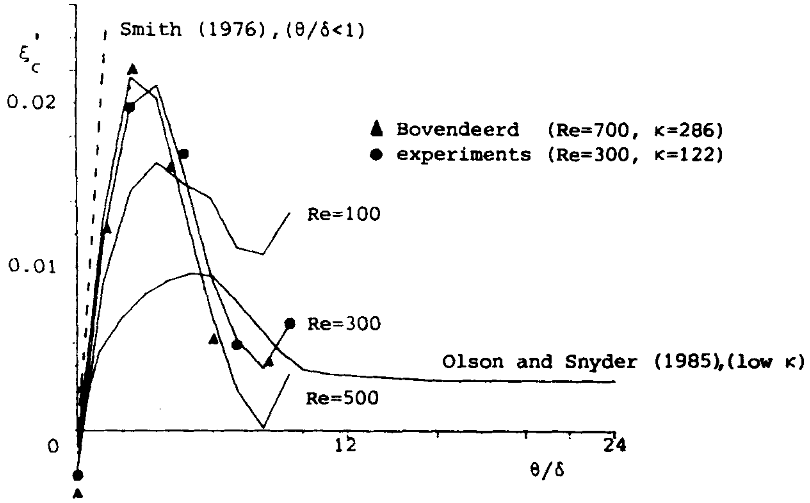

Figure 7. The dimensionless mean axial vorticity in the curved tube ($\delta = 1/6$) as a function of θ/δ as calculated for $Re = 100$, 300 and 500 ($\kappa = 41$, 122 and 204) and measured for $Re = 300$ ($\kappa = 122$), together with the results of Smith,[11] Olson and Snyder[9] and Bovendeerd *et al.*[10]

shifted slightly in this direction, both effects pointing to an upstream influence of the bend. The same upstream influence is found in the experiments. At $\theta = \pi/8$ the flow experiences the interaction of convective inertial, viscous and centrifugal forces.[30] In the central core of the tube, where the axial velocities are large, the centrifugal force dominates, resulting in a secondary flow towards the outer bend. Near the walls of the tube the centrifugal forces are less important and a circumferential back flow to the inner wall is found. In consequence of this phenomenon, the maximum of the axial velocity shifts towards the outer bend. In accordance with the analytical approximation for $\theta/\delta < 1$ made by Smith,[11] this initial behaviour is nearly independent of the Reynolds number. The initial increase of the circulation found here agrees quite well with the solution of Smith (see Figure 7). At $\theta = \pi/4$ the influence of the secondary motion as described above is clearly visible in the axial velocity distribution. The maximum of the axial velocity is convected further to the outer bend. At higher Reynolds numbers, where the convective terms are more important, 'C-shaped' isovelocity contours of the axial velocity component are found in accordance with the observations of, for instance, Agrawal *et al.*[6] and Olson and Snyder.[9] At the next axial station ($\theta = 3\pi/8$) the dependence on the Reynolds number becomes even clearer. For $Re = 100$ the velocity distribution does not differ much from the one found at the preceding axial location and an almost fully developed flow is found. For the higher Reynolds numbers ($Re = 300, 500$) the 'C-shaped' axial velocity profiles have become more pronounced. Furthermore, the secondary fluid motion is mainly restricted to a small boundary layer along the upper wall of the bend. Similar Reynolds number dependence is reported by Soh and Berger.[16] At $\theta = \pi/2$ the velocity distribution is strongly influenced by the upstream influence of the straight outflow region of the model. Here the secondary velocity distribution is characterized by an increase of the velocity component towards the outer bend; a reversed effect from that found at the entrance region of the bend. As seen in Figure 7, this increase does not agree with the general observations ($100 < \kappa < 500$, $4{\cdot}66 < 1/\delta < 8$) made by Olson and Snyder[9] for a 300° bend, and enables the flow to become fully developed. Finally, the increase of the Reynolds number leads to an increase of the maximum axial vorticity which, furthermore, is reached at smaller axial positions. The experiments of Bovendeerd *et al.*[10] and the observations made by Olson and Snyder[9] confirm this observation.

With respect to the applicability of the numerical model to three-dimensional flow problems, the following remarks are made. The agreement between the experimental and numerical results indicates that the finite element method applied offers an accurate tool for three-dimensional flow simulations. Although a relatively coarse mesh was used and although the number of pressure unknowns, and thus of constraints for divergence freedom (4), is small compared with that of the velocity, the results seem to be quite accurate. At $Re = 500$, however, the solution becomes slightly 'wiggly' (see Figure 5), and for higher Reynolds numbers ($Re = 700$) the solution procedure failed to converge at all, so finer meshes should be applied in that case. For the finite element mesh applied here, about 25 h CPU and about 2 days I/O were needed per Newton iteration (11 Newton iterations were needed to reach $Re = 500$) on a minicomputer (APOLLO DSP90). Therefore application of this solution procedure for three-dimensional bifurcation models demands more sophisticated computer capacity, such as array processing or supercomputers.

ACKNOWLEDGEMENT

We wish to thank H. J. de Heus for the work he performed obtaining the experimental data.

REFERENCES

1. D. E. Olson, '*Fluid mechanics relevant to respiration: flow within curved or elliptical tubes and bifurcating systems*', *Ph.D. Thesis*, University of London, 1971.
2. R. Brech and B. J. Bellhouse, 'Flow in branching vessels', *Cardiovasc. Res.*, **7**, 593–600 (1973).
3. F. W. LoGerfo, M. D. Nowak, W. C. Quist, H. M. Crawshaw and B. K. Bharadvaj, 'Flow studies in a model carotid bifurcation.', *Atherosclerosis*, **1**, 235–241 (1981).
4. A. J. Ward-Smith, *Internal Fluid Flow*, Clarendon Press, Oxford, 1982.
5. F. N. Van de Vosse, '*Numerical analysis of carotid artery flow*' *Ph.D. Thesis*, University of Technology, Eindhoven, 1987.
6. Y. Agrawal, L. Talbot and K. Gong, 'Laser anemometer study of flow development in curved circular pipes', *J. Fluid Mech.*, **85**, 497–518 (1978).
7. U. S. Choi, L. Talbot and I. Cornet, 'Experimental study of wall shear rates in the entry region of a curved tube', *J. Fluid Mech.*, **93**, 465–489 (1978).
8. D. E. Olson and B. Snyder, 'The growth of swirl in curved circular pipes', *Phys. Fluids*, **56**, 347–349 (1983).
9. D. E. Olson and B. Snyder, 'The upstream scale of flow development in curved circular pipes', *J. Fluid Mech.*, **150**, 139–158 (1985).
10. P. H. M. Bovendeerd, A. A. Van Steenhoven, F. N. Van de Vosse and G. Vossers, 'Steady entry flow in a curved pipe', *J. Fluid Mech.*, **177**, 233–246 (1987).
11. F. T. Smith, 'Fluid flow into a curved pipe', *Proc. Roy. Soc. A*, **351**, 71–87 (1976).
12. M. P. Singh, 'Entry flow in a curved pipe', *J. Fluid Mech.*, **65**, 517–539 (1974).
13. L. S. Yao and S. A. Berger, 'Entry flow in a curved pipe', *J. Fluid Mech.*, **67**, 177–196 (1975).
14. N. S. Liu, 'Developing flow in a curved pipe.', *INSERM-Euromech 92*, **71**, 53–64 (1977).
15. K. Stewartson, T. Cebeci and K. C. Chang, 'A boundary-layer collision in a curved duct', *Q. J. Mech. Appl. Math.*, **33**, 59–75 (1980).
16. W. Y. Soh and S. A. Berger, 'Laminar entrance flow in a curved tube', *J. Fluid Mech.*, **148**, 109–135 (1984).
17. C. Cuvelier, A. Segal and A. A. Van Steenhoven, *Finite Element Methods and Navier–Stokes Equations*, D. Reidel Publishing Co., Dordrecht/Boston/Lancaster/Tokyo, 1986.
18. F. Brezzi, 'On the existence, uniqueness and approximation of saddle point problems arising from Lagrangian multipliers', *RAIRO Anal. Numer.*, **8-R2**, 129–151 (1974).
19. V. Girault and P.-A. Raviart, *Finite Element Approximation of the Navier–Stokes Equations*, Springer-Verlag, Berlin/Heidelberg/New York, 1979.
20. M. Fortin, 'An analysis of the convergence of mixed finite element methods', *RAIRO Anal. Numer.*, **11**, 341–354 (1977).
21. M. Fortin, 'Old and new finite elements for incompressible flows', *Int. j. numer. methods fluids*, **1**, 347–364 (1981).
22. R. Temam, *Navier–Stokes Equations*, North-Holland Publishing Co., Amsterdam, 1977.
23. G. F. Caray and R. Krishnan, 'Penalty finite element method for the Navier–Stokes equations', *Comput. Methods Appl. Mech. Eng.*, **47**, 183–224 (1984).

24. J. N. Reddy, 'On penalty function methods in finite element analysis of flow problems', *Int. j. numer. methods fluids*, **2,** 151–171 (1982).
25. M. Fortin and A. Fortin, 'Newer and newer elements for incompressible flow', in R. H. Gallaher *et al.* (eds), *Finite elements in Fluids, Vol. 6*, Wiley, 1985.
26. M. Fortin and A. Fortin, 'Experiments with several elements for viscous incompressible flows', *Int. j. numer. methods fluids*, **5,** 911–928 (1985).
27. M. Crouzeix and P.-A. Raviart, 'Conforming and nonconforming finite element methods for solving the stationary Stokes equations I', *RAIRO Anal. Numer.*, **7,** 33–76 (1973).
28. F. N. Van de Vosse, A. Segal, A. A. Van Steenhoven and J. D. Janssen, 'A finite element approximation of the unsteady two-dimensional Navier–Stokes equations', *Int. j. numer. methods fluids*, **6,** 427–443 (1986).
29. A. Segal, 'Test problem for the $(Q_2^{(27)} - P_1)$ element', personal communication, 1986.
30. S. A. Berger, L. Talbot and L. S. Yao, 'Flow in curved pipes', *Ann. Rev. Fluid Mech.*, **15,** 461–512 (1983).